Earth and Planetary Science Letters 405 (2014) 244–256

Contents lists available at ScienceDirect

Earth and Planetary Science Letters

www.elsevier.com/locate/epsl

Coseismic fault zone deformation revealed with differential lidar: Examples from Japanese M_w ~7 intraplate earthquakes

Edwin Nissen [a,*], Tadashi Maruyama [b], J Ramon Arrowsmith [c], John R. Elliott [d], Aravindhan K. Krishnan [c], Michael E. Oskin [e], Srikanth Saripalli [c]

[a] Department of Geophysics, Colorado School of Mines, 1500 Illinois Street, Golden, CO 80401, USA
[b] Institute of Earthquake and Volcano Geology, National Institute of Advanced Industrial Science and Technology, Tsukuba Central 7, 1-1-1 Higashi, Ibaraki 305-8567, Japan
[c] School of Earth and Space Exploration, Arizona State University, ISTB4, 781 Terrace Road, Tempe, AZ 85287, USA
[d] COMET+ & Department of Earth Sciences, University of Oxford, South Parks Road, Oxford OX1 3AN, UK
[e] Department of Geology, University of California, Davis, 1 Shields Avenue, Davis, CA 95618, USA

ARTICLE INFO

Article history:
Received 24 May 2014
Received in revised form 21 August 2014
Accepted 26 August 2014
Available online 19 September 2014
Editor: P. Shearer

Keywords:
earthquake deformation
active tectonics
lidar

ABSTRACT

We use two recent Japanese earthquakes to demonstrate the rich potential, as well as some of the challenges, of differencing repeat airborne Light Detection and Ranging (lidar) topographic data to measure coseismic fault zone deformation. We focus on densely-vegetated sections of the 14 June 2008 Iwate–Miyagi (M_w 6.9) and 11 April 2011 Fukushima–Hamadori (M_w 7.1) earthquake ruptures, each covered by 2 m-resolution pre-event and 1 m-resolution post-event bare Earth digital terrain models (DTMs) obtained from commercial lidar providers. Three-dimensional displacements and rotations were extracted from these datasets using an adaptation of the Iterative Closest Point (ICP) algorithm. These displacements remain coherent close to surface fault breaks, as well as within dense forest, despite intervals of ~2 years (Iwate–Miyagi) and ~4 years (Fukushima–Hamadori) encompassed by the lidar scenes. Differential lidar analysis is thus complementary to Interferometric Synthetic Aperture Radar (InSAR) and sub-pixel correlation techniques which often break down under conditions of long time intervals, dense vegetation or steep displacement gradients. Although the ICP displacements are much noisier than overlapping InSAR line-of-sight displacements, they still provide powerful constraints on near-surface fault slip. In the Fukushima–Hamadori case, near-fault displacements and rotations are consistent with decreased primary fault slip at very shallow depths of a few tens of meters, helping to account for the large, along-strike heterogeneity in surface offsets observed in the field. This displacement field also captures long-wavelength deformation resulting from the 11 March 2011 Tohoku great earthquake.

© 2014 Elsevier B.V. All rights reserved.

1. Introduction

Over the past two decades, Interferometric Synthetic Aperture Radar (InSAR) and optical or SAR amplitude pixel matching techniques have enabled coseismic surface deformation to be mapped over wide regions and at dense spatial resolutions (e.g., Massonnet et al., 1993; Michel et al., 1999; van Puymbroeck et al., 2000). These data are crucial for identifying the causative faulting, resolving patterns of slip at depth, probing the mechanical properties of the fault zone, mapping the transfer of stresses onto neighboring faults, and interpreting the long-term record of earthquakes recorded in topography. However, these methods are hampered by certain restrictions. (1) They measure only particular components of the three-dimensional (3-D) deformation field. (2) C-band InSAR and sub-pixel correlation techniques often break down in regions with forest or agricultural cover. (3) While InSAR is powerful at detecting the far-field deformation of continental earthquakes caused by slip at depth, steep phase gradients and intense ground shaking often lead to loss of coherence within and along the fault zone itself, limiting our constraints upon the shallow slip distribution.

Differencing of pre- and post-earthquake topography offers rich potential for addressing these limitations. Airborne Light Detection and Ranging (lidar), also known as airborne laser swath mapping (ALSM), uses a laser ranging device, together with information on the position and orientation of the aircraft platform, to determine the x, y and z coordinates (within a global geodetic reference frame) of an uneven distribution of ground targets (a 'point

* Corresponding author.
E-mail address: enissen@mines.edu (E. Nissen).

http://dx.doi.org/10.1016/j.epsl.2014.08.031
0012-821X/© 2014 Elsevier B.V. All rights reserved.

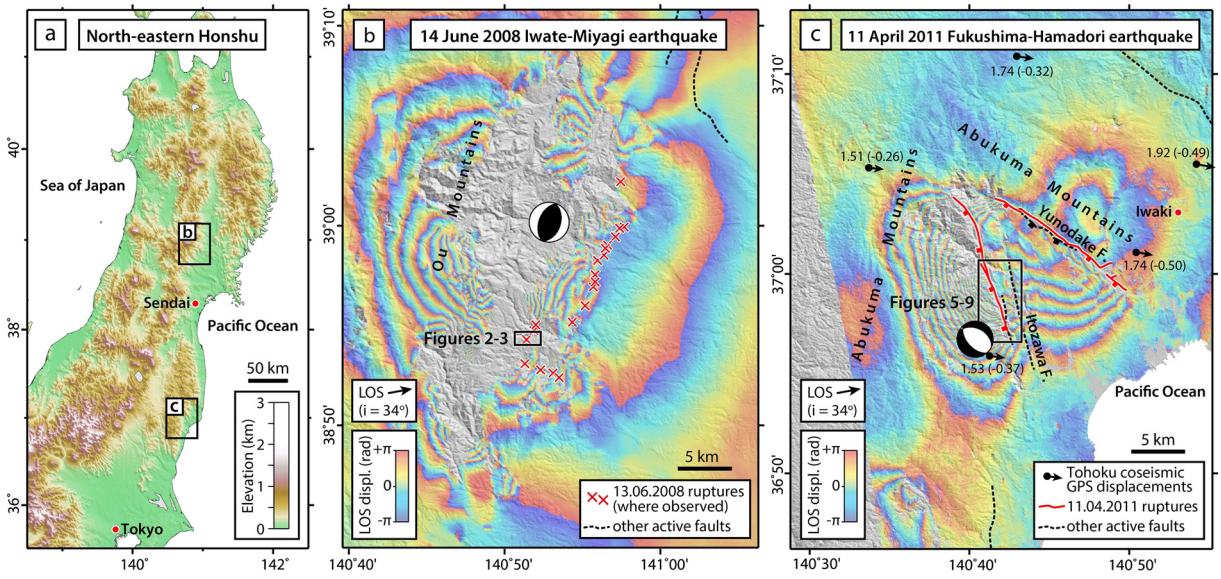

Fig. 1. (a) Topographic map of north-eastern Honshu, Japan. (b) The epicentral region of the 14 June 2008 Iwate–Miyagi earthquake (M_w 6.9) showing the Global CMT catalog focal mechanism, the locations of mapped surface ruptures from Matsu'ura and Kase (2010) and Toda et al. (2012), and a coseismic interferogram constructed from ALOS PALSAR ascending track 402 scenes from 21 June 2007 and 23 June 2008 (using JPL/Caltech ROI-PAC software). i is the line-of-sight (LOS) incidence angle (measured from the vertical) and 2π radians in LOS displacement is equivalent to the radar half-wavelength of 11.8 cm (with positive increasing values indicating motion away from the satellite). (c) The epicentral region of the 11 April 2011 Fukushima–Hamadori earthquake (M_w 7.1) with mapped surface ruptures from Mizoguchi et al. (2012) and Toda and Tsutsumi (2013), the GCMT focal mechanism, and a coseismic interferogram constructed from ALOS PALSAR ascending track 304 scenes from 3 March and 18 April 2011. The fringe pattern near the SW corner of the figure results from an earlier M_w 5.8 (M_j 6.1) earthquake on 19 March 2011 (Kobayashi et al., 2012). We also plot coseismic GPS displacements for the Tohoku earthquake from Ozawa et al. (2011); numbers refer to lateral (and vertical) displacements in meters. Other active faults are from Nakata and Imaizumi (2002).

cloud') to a precision of a few centimeters (Carter et al., 2007; Glennie et al., 2013). Modern lidar surveys can map wide regions at densities of several points/m^2 or higher and can also record multiple returns from a single laser pulse, such as from vegetation and the underlying ground surface. This capability allows canopy to be removed from lidar point clouds, and has been used to reveal previously unidentified fault scarps in densely forested regions (Haugerud et al., 2003; Cunningham et al., 2006; Hunter et al., 2011; Barth et al., 2012; Z. Lin et al., 2013; Langridge et al., 2014).

As the point spacing in modern lidar datasets is finer than the scale of slip and displacement in large earthquakes, differencing of 'before' and 'after' fault zone topography should reveal 3 dimensional (3-D) coseismic surface displacements with minimal loss of coherence in vegetated areas or in rupture zones. An explosion of lidar surveying in the past decade provides a topographic baseline for future differencing opportunities along many active faults, particularly in the western US (e.g., Bevis et al., 2005; Prentice et al., 2009). However, demonstration of this emerging new application for airborne lidar has so far been restricted by a lack of high quality paired datasets on which to test them. The 2010 El Mayor–Cucapah earthquake rupture in northern Mexico is the only earthquake with complete pre- and post-lidar coverage, but 3-D analysis of the deformation field is made difficult by the unusually sparse density (~0.013 points/m^2) of the pre-event dataset (Oskin et al., 2012; Glennie et al., 2014). Experiments on southern California lidar datasets deformed with simulated earthquakes of known displacements reveal what should be possible with higher density point clouds (Borsa and Minster, 2012; Nissen et al., 2012). In addition, all of these studies focus on semi-arid landscapes where vegetation cover is not a serious issue for lidar differencing, as it will be in many future cases.

In this paper, we exploit two, newly-available, paired lidar datasets to map 3-D fault zone deformation along portions of two recent earthquake ruptures in Japan (Fig. 1). Both events occurred in regions with dense forested cover, allowing us to explore lidar differencing in more testing conditions than was previously possible. We also address the need to incorporate third party lidar datasets which were not optimized for earthquake studies and for which important data collection and processing metrics are unavailable (see also Glennie et al., 2014). Despite these challenges, the Japanese case studies presented here demonstrate some of the potential insights from this new geodetic technique. A particularly promising application, best illustrated by our second case study, is to use coherent lidar displacements from the interior part of the fault zone to help bridge a critical observational gap between surface faulting offsets (measured in the field over meter-scale apertures) and slip occurring at depths of a few kilometers (such as is routinely inferred using InSAR over kilometer-scale apertures). Discrepancies in these measurements have important implications for understanding the mechanical behavior of fault zones and for interpreting their geomorphology (e.g., Simons et al., 2002; Fialko, 2004; Fialko et al., 2005; Copley et al., 2012; Dolan and Haravitch, 2014).

2. 2008 Iwate–Miyagi earthquake (M_w 6.9)

This earthquake struck north-eastern Honshu on 14 June 2008, in a mountainous region along the border of the Iwate and Miyagi prefectures, ~400 km north of Tokyo (Fig. 1a). Ascribed a local magnitude (M_{jma}) of 7.2 by the Japanese Meteorological Agency (JMA) and a moment magnitude (M_w) of 6.9 by the Global Centroid Moment Tensor (GCMT) catalog, this was the largest inland earthquake in Japan since the devastating 1995 Kobe event (M_{jma} 7.3, M_w 6.9), and it led to 23 people dying or going missing, ~500 injuries, and heavy damage to more than 100 buildings. The earthquake also triggered more than 4100 mapped landslides and debris flows which contributed greatly to the loss of life and property in the area (Yagi et al., 2009).

Source models based on near-field high rate GPS and strong motion data show that the earthquake involved predominantly reverse slip along a ~40 km-long, NNE-striking and WNW-dipping

fault (Ohta et al., 2008; Yokota et al., 2009; Suzuki et al., 2012; Lucca et al., 2012). InSAR models for the earthquake are in general agreement, but also incorporate slip on a conjugate ESE-dipping fault in the central part of the fault zone (Takada et al., 2009; Abe et al., 2013). According to these models, peak slip was 1–3 m in the northern part of the fault zone and 3.5–6.5 m in the southern part and occurred at a depth of 2–5 km.

The main causative fault, which had not been identified prior to the earthquake, broke along the eastern flank of the Ou Mountains (Fig. 1b), a range that is mainly composed of Miocene–Quaternary volcanic and sedimentary rocks (Toda et al., 2012). InSAR measurements were hindered by poor coherence in much of the hanging-wall as well as along parts of the surface rupture, including the entire area of double lidar coverage (Fig. 1b). Field observations were also hampered by steep, forested terrain in much of the fault zone and only a few, isolated field measurements of surface slip were made (Matsu'ura and Kase, 2010; Toda et al., 2012). Vertical fault offsets are mostly <0.5 m, despite the inference from InSAR modeling of several meters of reverse slip along the fault plane at 2–5 km depth (Takada et al., 2009; Abe et al., 2013). An exception to this general pattern was observed in the southern part of the fault zone, where Toda et al. (2012) used terrestrial lidar measurements to document right-lateral offsets of up to 7 m and vertical offsets of up to 4 m along a $\sim$1 km-long, E–W-striking fault scarp. This section of surface rupture lies within the area of repeat lidar coverage focused on in this paper.

2.1. Iwate–Miyagi lidar differencing

In September 2006 the commercial surveying company Kosukai Kogyo Co., Ltd. (http://www.kk-grp.jp/) acquired lidar data over several watersheds in the epicentral region of the future earthquake, primarily for the purpose of land management. These data were collected from an aeroplane platform, which flew at an average height of 2600 m above ground level (AGL) and carried a 32 kHz Leica Geosystem ALS40 scanner. This survey generated ground return densities averaging $\sim$0.25 points/m^2. After the earthquake struck, another commercial lidar provider, Aero Asahi Corporation (http://www.aeroasahi.co.jp/), surveyed parts of the rupture zone during several flights in June, July, August and September 2008. Deploying a 70 kHz Optech ALTM3100 scanner from a helicopter platform at $\sim$1000 m AGL, they were able to generate average point densities of $\sim$4 points/m^2.

We identified a small (1700 m $\times$ 900 m) region within the southern part of the fault zone that was mapped in both surveys (black rectangle, Fig. 1b). We obtained pre- and post-event, gridded, bare earth digital terrain models (DTMs) – shown in Figs. 2a and 2b – although we were not provided information about the steps taken to rasterize the raw points clouds and remove vegetation. The pre- and post-earthquake DTMs have resolutions of 2 m and 1 m, respectively, and both are registered in Japan Plane Rectangular Coordinate System X (in meters), though we have no information about the differential GPS ground control used during surveying, nor any accuracy validation. Most of the area covered by the lidar is densely forested (Fig. 2c). Within the scene boundaries, there is no clear evidence for the presence of an active fault in the pre-event DTM. The post-event DTM includes a $\sim$1 km-long fault scarp (Figs. 2d, 2e), which is the same section of surface faulting described in detail by (Toda et al., 2012). The eastern portion of the scarp faces south and the western portion faces north. Two major, deep-seated landslides triggered by the earthquake also lie within or partly within the focus area of this study. Part of the Aratozawa landslide – the largest of those triggered by the earthquake with a volume of $\sim$70 million cubic meters (Yagi et al., 2009) – is covered by the SW corner of the scene (Figs. 2b, 2c), while the Sanhazama landslide lies in the scene center (Figs. 2b, 2c, 2f).

For an initial analysis we subtract the pre-earthquake DTM from the post-earthquake DTM (e.g., Oskin et al., 2012). Although this leads to aliasing of tectonic horizontal deformation, the elevation change results are at the resolution of the DTMs — in contrast with the 3-D displacements we later determine, which are much coarser resolution — and therefore have the potential to reveal interesting short-wavelength deformation signals. In this instance, large negative and positive elevation changes are revealed in the central parts of the scene related to the scarp and toe of the Sanhazama landslide, respectively (Fig. 3a). The landslide has in turn blocked and dammed the eastward-flowing Sanhazama River, which consequently displays positive elevation changes of a few meters along its upper course. The scarp of the Aratozawa landslide in the SW corner of the scene is also characterized by strong negative elevation changes. Linking the two landslide scarps, the $\sim$1 km-long fault scarp mapped by Toda et al. (2012) is also marked by a faint discontinuity in elevation difference values. However, the simple DTM elevation differencing does not measure horizontal motions and it is therefore difficult to discern additional information about coseismic displacements from this map. Independently, Mukoyama (2012) applied particle image velocimetry (PIV) to lidar slope maps to obtain horizontal displacements across this area (using a different post-event dataset to the one we use), but this method does not account for vertical changes.

To construct the 3-D surface deformation field, we used the implementation from Nissen et al. (2012) of the Iterative Closest Point (ICP) algorithm (Besl and McKay, 1992; Chen and Medioni, 1992). It computes 3-D surface displacements and rotations by iteratively minimizing closest point distances between local square subsets ("cells") of the pre-event ("source") and post-event ("target") data (Fig. 4). The resulting, cumulative rigid-body transformation represents the local displacement and rotation that most closely aligns the pre-event cell topography to the post-event equivalent. The choice of cell dimension must balance the desire for finer resolution against the requirement that each cell contain enough topographic heterogeneity for an accurate alignment to be achievable. Pairs of cells that contain planar arrays of points can, of course, be aligned in any number of ways and so in very smooth, flat or planar areas ICP results may be meaningless (for example, ICP displacements computed by Glennie et al., 2014 for the El Mayor–Cucapah earthquake are spurious on the smooth playa of Laguna Salada, but mostly retain coherence across rougher planar surfaces such as alluvial fans and dry river beds). In addition, larger cell sizes risk there being significant internal strain arising from the displacement field, which would prevent alignment through the ICP rigid body transformation. However, Nissen et al. (2012) showed that realistic elastic deformation gradients have negligible effects on computed ICP displacements for the cell sizes considered in this study.

Taking these factors into consideration and after experimentation, we used a cell size of 50 $\times$ 50 m. The target cells also included an additional 10 m-wide overlapping border in order to spatially encompass the coseismic displacement and thus ensure that topographic features in each pre-event cell are contained within the post-event cell (Fig. 4). While this results in a 20 m overlap between adjacent post-event cells, there is no overlap between adjacent pre-event cells and each computed displacement is thus independent from neighboring ones. Although the method is easily applied to irregularly-spaced point clouds, here we were restricted to using the regularly-spaced nodes of the DTMs. This potentially introduces a bias in computed displacements, because certain alignments of regularly-spaced grids achieve closer horizontal closest point distances than others. For this reason, we chose to use point-to-plane ICP (Chen and Medioni, 1992) which

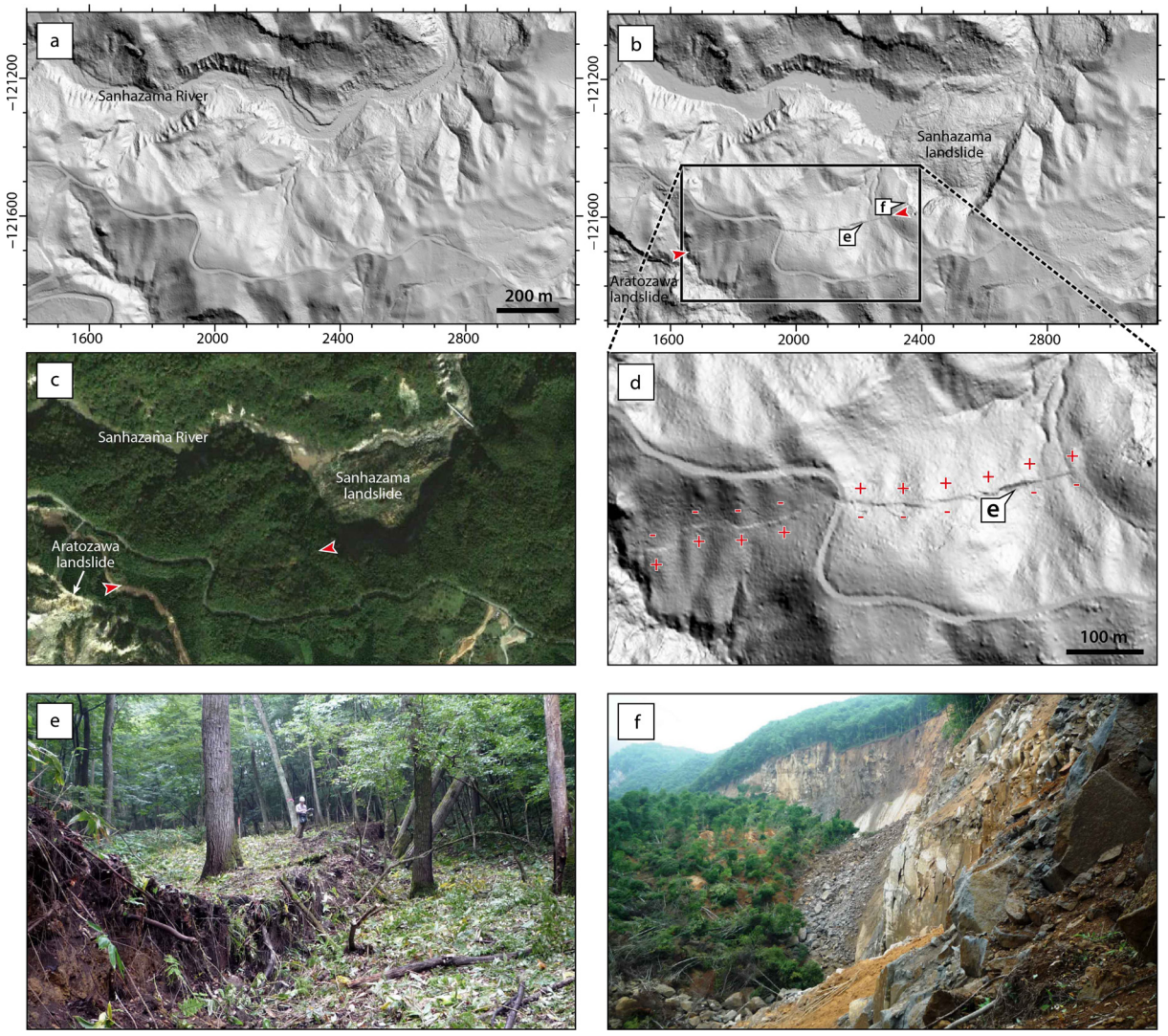

Fig. 2. (a) Pre- and (b) post-earthquake airborne lidar DTMs spanning the 2008 M_w 6.9 Iwate–Miyagi earthquake, artificially illuminated from the NE with *x* and *y* coordinates in meters (Japan Plane Rectangular Coordinate System X). In (b), red arrows point to the ends of the fault scarp. (c) Post-earthquake Google Earth image of the same scene captured on 15 October 2009. Red arrows again point to ends of the rupture trace, which is obscured by forest cover in this image. (d) Fault scarp in (b) shown at greater magnification. The earthquake scarp is marked in by red pluses on the locally-upthrown side and minuses on the downthrown side. (e) Photograph of surface rupture, facing approximately ENE with geologist for scale. Note dense forest canopy. Photograph location shown in (b) and (d). (f) Photograph of the landslide scarp at the head of the Sanhazama landslide, facing approximately E. Photograph location shown in (b). (For interpretation of the references to color in this figure legend, the reader is referred to the web version of this article.)

minimizes distances between each source point and the tangential plane at its target point.

The ICP differencing clearly reveals the 3-D coseismic displacement field across the scene (Fig. 3b), in stark contrast with the simple DTM elevation differencing (Fig. 3a). As outlined earlier, in this simple implementation of the ICP algorithm the displacement value for each cell is obtained independently from those of its neighbors. This gives us confidence that the smoothly-varying displacements observed across most of the scene are genuine. It also implies that there is no limit to the displacement gradients resolvable between adjacent cells, as long as the internal cell strain is not so large that ICP cannot compute a meaningful rigid-body alignment in the first place (as discussed earlier). In practice this means that ICP yields mostly spurious displacements for cells that contain the fault scarp – these have been removed from Fig. 3b – but yields coherent displacements for cells in very close proximity to the surface break including neighboring ones. This is in stark contrast with conventional InSAR, where line-of-sight displacement gradients of more than one radar half-wavelength (typically a few centimeters) per pixel (typically a few tens of meters) result in incoherent noise. In this example, InSAR imagery is completely decorrelated within the extents of the lidar scene (Fig. 1b; Midorikawa and Miura, 2008; Takada et al., 2009). The improved spatial coherence of the lidar displacement field is impressive considering the fact that these measurements encompass a ∼2 year interval compared to the ∼1 year timespan of the interferogram shown in Fig. 1b.

In addition to the DTM cells which contain the fault scarp, those encompassing the two landslides and the dammed river also involve a change in internal cell shape, rendering ICP alignments spurious. Displacements in these cells are consequently eliminated from Fig. 3b. These areas are instead best characterized by the DTM elevation difference map in Fig. 3a. There remains the potential to use ICP and PIV to detect block surface motions occurring within deep-seated landslides (Teza et al., 2007; Aryal et al., 2012), but the two contained within our scene each involved incoherent collapse of the hillside rendering these methods challenging or even impossible.

Discounting cells containing the fault scarp or which cover the two landslides or the dammed river, ICP results appear coherent

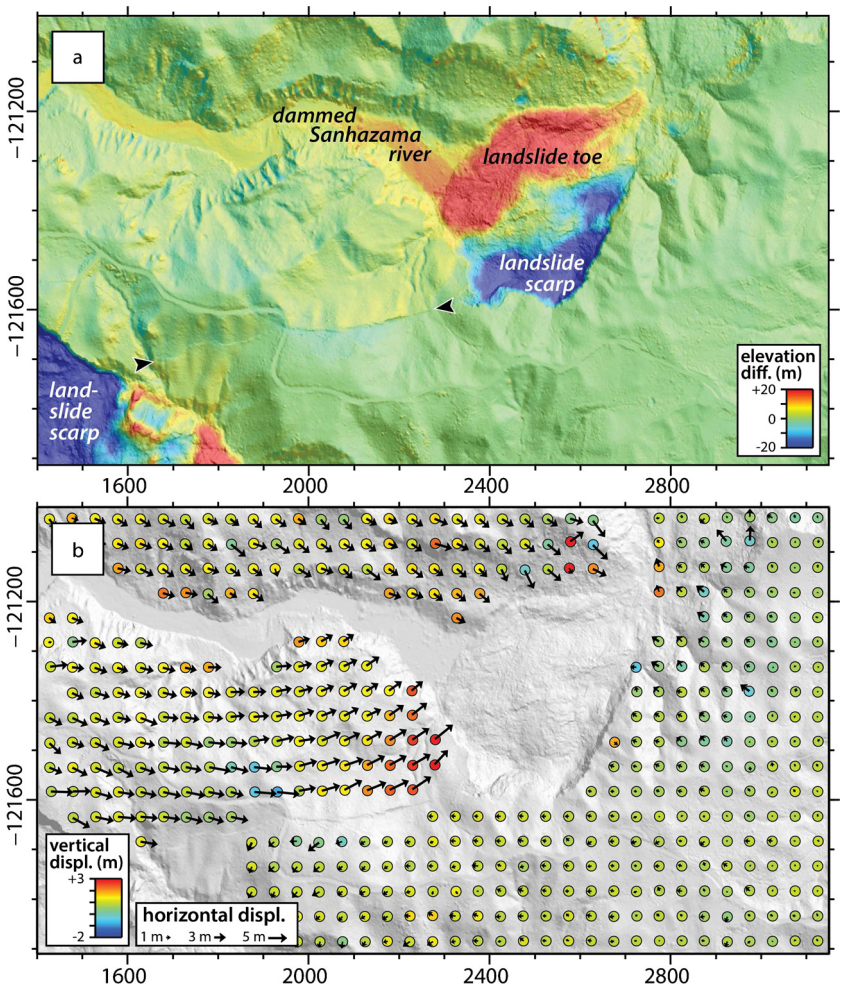

Fig. 3. (a) Elevation change for the 2008 M_w 6.9 Iwate–Miyagi earthquake determined by subtracting pre-earthquake DTM from post-earthquake DTM. Black arrows point to the ends of the rupture trace. (b) ICP differencing results: arrows are horizontal displacements and colored circles are vertical displacements. The entire extent of this map is incoherent in InSAR imagery (Fig. 1b).

across the scene with very few obviously spurious displacements (Fig. 3b). The NW side of the fault generally translates eastwards relative to the SE side, indicating significant right-lateral slip, consistent with published focal mechanisms and fault models (e.g., Takada et al., 2009). Vertical displacements in cells lying either side of the E–W trending fault scarp also indicate a component of dip slip, with a N-side up sense along the eastern part of the scarp, in agreement with field observations (Toda et al., 2012). In the region between the scarp and the dammed Sanhazama river, material rotates anticlockwise around a vertical axis such that adjacent to the landslide scar, surface displacements are to the NE. However, north of the dammed river, displacements are uniformly towards the SE. The resultant discontinuity in displacements across the Sanhazama river may reflect (1) shallow faulting along the trend of the river channel or (2) NE-directed slumping of the southern flank of the Sanhazama valley. Superficially, our horizontal displacement field resembles the one obtained from particle image velocimetry (Mukoyama, 2012).

3. 2011 Fukushima–Hamadori earthquake (M_w 7.1)

This M_w 7.1 (M_{jma} 7.0) earthquake occurred in the Abukuma Mountains west of Iwaki city, southern Fukushima prefecture, on 11 April 2011 (Fig. 1c). It was the largest of a swarm of shallow normal faulting earthquakes associated with E–W extension of northern Honshu during and after the 11 March 2011 Tohoku great earthquake (Kato et al., 2011; Imanishi et al., 2012). Field mapping (Mizoguchi et al., 2012; Toda and Tsutsumi, 2013) and InSAR imagery (Kobayashi et al., 2012; Fukushima et al., 2013) indicate that the earthquake produced two distinct, subparallel surface ruptures, apparently simultaneously (Fig. 1c). Both occurred along previously recognized faults and involved predominantly down-to-the-west normal slip.

Detailed mapping of both rupture strands was undertaken by Mizoguchi et al. (2012) and Toda and Tsutsumi (2013). We complement their observations with our own slip measurements (collected by T.M. in middle April–June 2011) within the area of repeat lidar coverage (Figs. 1c, 5). The 16 km-long eastern rupture involved up to 0.9 m of vertical offset along the Yunodake Fault, which forms a SW-facing escarpment separating Cretaceous metamorphic and igneous rocks of the Abukuma Mountains to the NE from a wedge-shaped half-graben filled with Neogene sedimentary rocks to the SW (Fig. 1c). However, this fault lies outside the region in which we have obtained pre- and post-event lidar data so we henceforth concentrate on the western rupture.

Here, the earthquake generated a ~14 km-long scarp along the NNW-trending Itozawa fault, which cuts through Cretaceous metamorphic rocks along the eastern margin of the Abukuma Mountains. Vertical offsets of up to 2.2 m were measured, up to the ENE, thereby acting to reverse the local topography and causing several E-flowing streams to pond against the fault scarp. Smaller components of strike-slip were also documented, with a left-lateral sense along the northern part of the rupture and a right-lateral

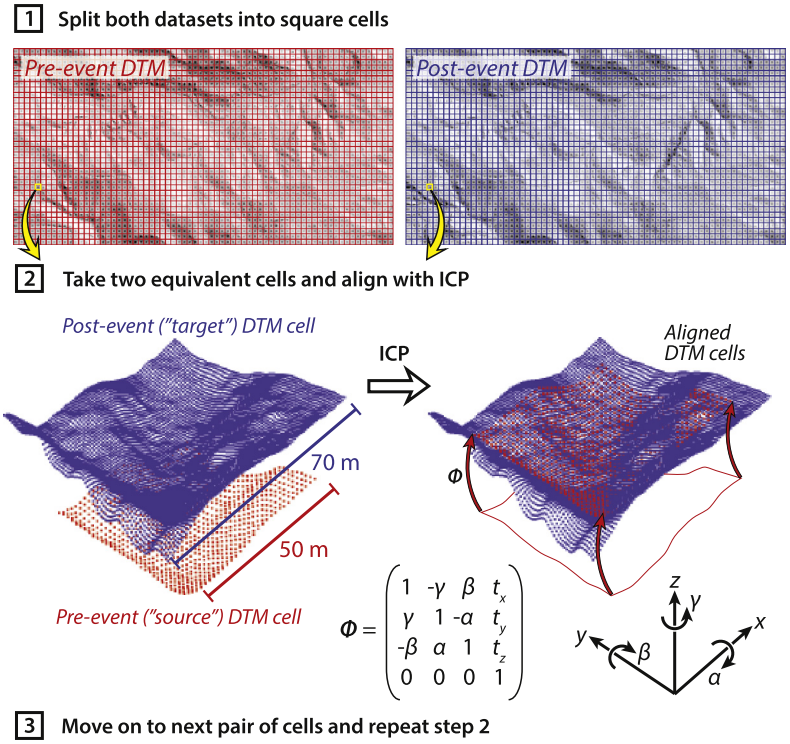

Fig. 4. An outline of our Iterative Closest Point (ICP) method for aligning pre- and post-event DTM cells. In step 2, the rigid body transformation ϕ that minimizes closest point distances between the pre- and post-event DTM nodes comprises translations t_x, t_y and t_z in the x, y and z directions, and rotations α, β and γ about the x, y and z axes.

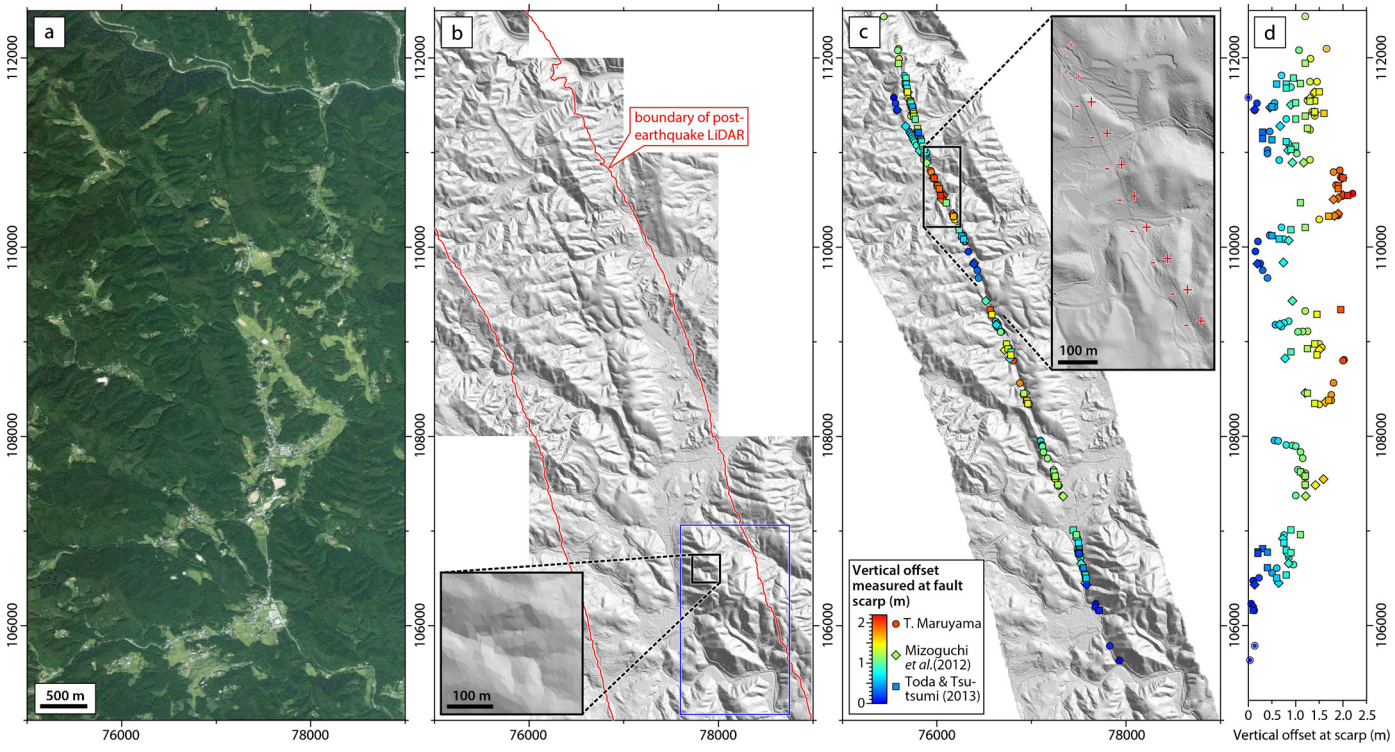

Fig. 5. (a) Pre-event Google Earth image captured on 17 September 2005, illustrating the dense vegetation within much of the study area. (b) Pre- and (c) post-earthquake airborne lidar DTMs spanning the 2011 M_w 7.1 Fukushima–Hamadori earthquake, artificially illuminated from the NE with x and y coordinates in meters (Japan Plane Rectangular Coordinate System IX). In (b), the blue rectangle marks an area which contains large triangular artefacts, as illustrated in the inset box. In (c), colored symbols show field measurements of vertical offset along the Itozawa rupture, styled according to the different observers. The inset shows a detailed view of the section containing the greatest measured vertical offset, with red pluses and minuses marking the upthrown and downthrown sides of the fault scarp, respectively. (d) Field measurements of vertical surface offset plotted by their northing coordinate, with colored symbols as in (c). The large scatter in slip values north of 111 000 is partly due to a local split of the fault scarp into two strands. (For interpretation of the references to color in this figure legend, the reader is referred to the web version of this article.)

sense along the southern part. Most bedrock fault plane exposures indicate steep dips of >70°, consistent with the linear trace of the fault across undulating topography. However, the fault dip at seismogenic depths is ambiguous: InSAR modeling by Kobayashi et al. (2012) points to a planar fault with a dip of 57° whereas Fukushima et al. (2013) propose a listric fault geometry with a shallow (∼30°) dip at depth and a steeper (∼72°) dip at the surface.

The largest vertical offsets measured in the field are generally concentrated along the southern half of the Itozawa rupture, within the area of repeat lidar coverage (Fig. 5). Measurements by Mizoguchi et al. (2012), Toda and Tsutsumi (2013) and by T. Maruyama are in close agreement and indicate a notable along-strike variation in offset magnitude (Figs. 5c, 5d). There are two distinct scarp sections accommodating offsets of ∼2 m separated by a ∼0.5 km section in which most are <0.5 m; in some places there is also more localized scatter, with variations of >1 m in vertical scarp offset occurring over distances of <100 m. Paleoseismic trenching along the southern part of the rupture indicates that the penultimate event occurred ca. 12–17 kyr before present and is consistent with a slow fault slip-rate (Toda and Tsutsumi, 2013).

3.1. Fukushima–Hamadori lidar differencing

The two companies that collected pre- and post-earthquake lidar data along the Itozawa Fault are the same as those for the earlier Iwate–Miyagi earthquake. Kosukai Kogyo collected a regional lidar dataset during several flights in late 2006 and early 2007, using a 30 kHz Leica Geosystem ALS50 scanner deployed from an aeroplane platform operating at ∼2500 m AGL. Their surveys generated ground return densities averaging ∼0.25 points/m^2. In May 2011, shortly after the earthquake, Aero Asahi surveyed a 2 km-wide swath along the Itozawa rupture from a helicopter platform at 750 m AGL equipped with a 100 kHz Optech ALTM3100 scanner, achieving average densities of ∼7 points/m^2. As in the case of the Iwate–Miyagi earthquake, much of the epicentral region is densely forested (Fig. 5a).

We acquired the 2 m-resolution pre-event bare earth DTM shown in Fig. 5b and the 1 m-resolution post-event DTM shown in Fig. 5c, both registered in Japan Plane Rectangular Coordinate System IX (in meters). Again, we have no information about surveying accuracies nor about the precise steps taken to generate the bare Earth models. Though everywhere rasterized at a 2 m spacing, the pre-event DTM is in some places represented by conspicuous triangular facets with dimensions of up to a few tens of meters. The facet vertices presumably reflect a triangular irregular network (TIN) constructed in areas containing sparse ground returns and are most prominent in the SE part of the scene (Fig. 5b). The post-event DTM captures the fresh fault scarp clearly (inset, Fig. 5c).

The two lidar datasets span both the 11 April 2011 Fukushima Hamadori earthquake and the preceding 11 March 2011 Tohoku great earthquake. Nearby GPS stations of the GPS Earth Observation Network (GEONET) shifted 1.5–1.75 m in a roughly easterly direction and subsided by 0.25–0.5 m during the Tohoku event (Fig. 1c), and shifted a further ∼0.2 m eastwards during the subsequent two week post-seismic interval (Ozawa et al., 2011). Any differences between the two lidar datasets therefore reflect a combination of (1) deformation due to the distant Tohoku great earthquake, which in our relatively narrow focus area consists of approximately uniform shifts to the east and vertically downwards, and (2) localized displacements caused by the Fukushima–Hamadori earthquake. Although this is also true of the coseismic interferogram shown in Fig. 1c, the >4 year interval between the two lidar scenes is much longer than typical InSAR timespans.

Elevation differences computed from a straightforward subtraction of the pre-event DTM from the post-event DTM generally show more positive values east of the surface rupture and more negative values west of it (Fig. 6a), consistent with the down-to-the-west sense of normal slip observed in the field and with InSAR. However, these values also exhibit a short-wavelength variability which is correlated with local slope aspect and gradient. As with the earlier case study, this reflects the fact that lateral displacements (caused by both the Tohoku and Fukushima–Hamadori earthquakes) are not accounted for by this most simple of differencing strategies.

We undertook 3-D differencing of the two datasets using the same implementation as was used in Section 2.1 (point-to-plane ICP with a 50 × 50 m source cell size and 70 × 70 m target cell size; Fig. 4). Resultant vertical displacements reveal smoothly-varying patterns of uplift and subsidence (Fig. 6b), in contrast with the more spatially-heterogeneous DTM elevation differences (Fig. 6a). We further illustrate this point using histogram plots which show a much greater spread of elevation difference values (inset, Fig. 6a) than of vertical ICP displacements (inset, Fig. 6b). Fault-perpendicular swath profiles through the vertical displacements exhibit a clear step across the mapped surface rupture, although there is significant local scatter (Fig. 6c). In general, ∼90% of these values lie within ±50 cm of linear trends through the footwall and hanging wall displacements, and a small number of the outliers are clearly spurious. However, displacements in the southern part of the scene – within the dashed rectangle on Figs. 6a and 6b and including parts of swaths F–F′ and G–G′ in Fig. 6c – are noisier still. This area is where prominent triangular facets were introduced during the construction of the pre-earthquake DTM (inset, Fig. 5b), probably due to a local scarcity of ground returns in the original surveys. These artefacts cause significant differences in the internal shape of equivalent pre- and post-earthquake cells, leading in turn to spurious or erroneous ICP displacements.

In contrast with the vertical deformation, E–W and N–S ICP displacements (Figs. 7a, 7b) lack a clear discontinuity across the fault. For a steeply dipping normal faulting event, vertical displacements are likely to dominate and it seems likely that the horizontal signature of the Fukushima–Hamadori earthquake is simply lost in the noise. In addition, horizontal displacements appear noisier than the vertical ones, with only ∼60% of the x and y displacements lying within ±50 cm of the local linear trend, compared with ∼90% for the vertical displacements. This is also shown by the histograms of horizontal x and y displacements (insets to Figs. 7a and 7b), which are noticeably larger than that of the vertical displacements (inset, Fig. 6b). Presumably this reflects the fact that slope gradients are usually <1, such that any mistakes in alignment effect displacements in the z direction less than those in x and y directions. Another possible contributing factor is that lidar ground returns typically have more precise z coordinates than x and y ones (e.g., Toth et al., 2007).

Nevertheless, E–W displacement values in Fig. 7a are clustered around +2 m (rather than around zero), which presumably reflects the approximately uniform eastwards shift of the area during and immediately after the 11 March Tohoku earthquake. This value is close to coseismic and early postseismic displacements recorded at the nearest GPS stations, as described earlier (Ozawa et al., 2011; Fig. 1b).

Finally, we are able to check that the apparent scatter in our lidar displacements is genuine noise (rather than short-wavelength deformation) by comparing them with overlapping InSAR line-of-sight (LOS) displacements, which could be measured across much of the area of interest, if not right up to the surface faulting. We first projected the ICP x, y and z displacements onto the InSAR satellite LOS direction (Fig. 8a; see caption for details) and

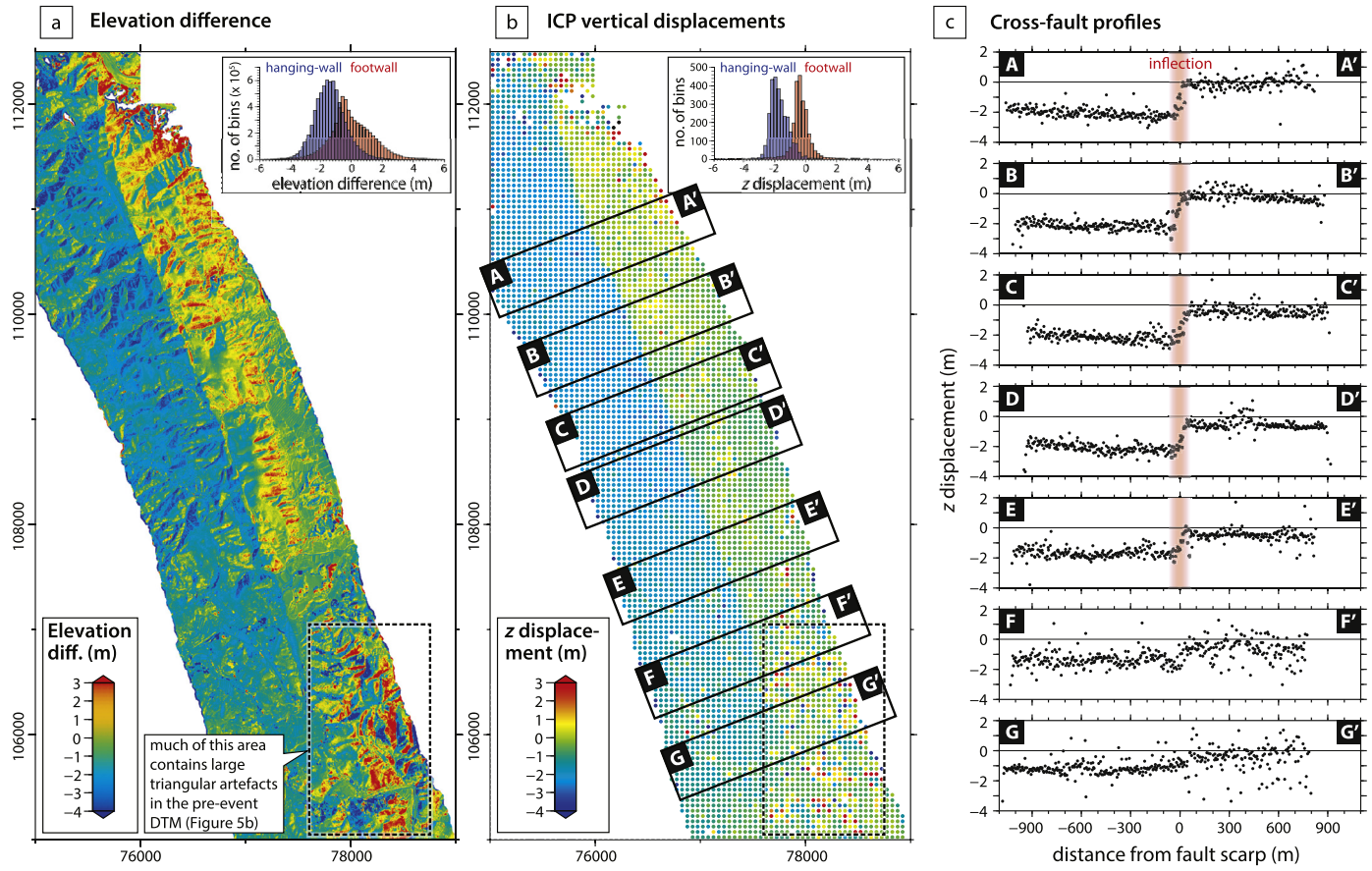

Fig. 6. (a) Elevation change determined by subtracting pre-event DTM from post-event DTM. The dashed rectangle is the area in which the pre-event DTM contains large triangular artefacts (see for example the inset to Fig. 5b). Inset shows a histogram of elevation difference values, constructed using a bin width of 0.2 m and separated into footwall values in red and hanging-wall in blue. (b) Vertical displacements obtained through ICP differencing of pre- and post-event DTMs. Inset shows a histogram of vertical displacements, constructed in the same manner as the inset to (a). (c) Cross-fault swath profiles through ICP vertical displacements. Swaths have fault-parallel widths of 500 m and are shown in (b). The inflection about the surface rupture is marked in red on profiles A–E, although its precise width is difficult to discern due to scatter in the data.

then compared these with 30 m-resolution LOS displacements from the filtered, unwrapped InSAR interferogram (Fig. 8b). Profiles through each dataset show the same general trend, but confirm that most of the apparent scatter in the ICP displacements is indeed noise.

4. Discussion

The work presented in this paper illustrates some of the challenges of lidar differencing but also its rich potential. Displacements measured with ICP contain significant noise and we discuss its source, and potential strategies for removing it, in Section 4.1. Nevertheless, the resulting displacement fields are largely coherent even at distances of less than a few hundred meters from the surface fault breaks, in contrast with SAR interferograms and despite the much longer intervals spanned by the lidar scene pairs. For this reason, ICP displacements from repeat topography constitute an ideal dataset for probing shallow earthquake slip, a point which we discuss in detail in Section 4.2.

4.1. Technical issues with respect to lidar differencing

The ±50 cm scatter in ICP vertical displacements is significantly larger than RMS errors of ∼4 cm (for vertical displacements) and ∼20 cm (for both E–W and N–S displacements) determined by testing the same differencing procedure on airborne lidar point clouds deformed with simulated earthquakes of known displacement (Nissen et al., 2012). This discrepancy can help us identify possible sources of noise in the Japanese earthquake examples, and to consider ways of reducing scatter in future lidar differencing studies.

The experiments by Nissen et al. (2012) were undertaken on pre-event and simulated post-event data collected on separate but overlapping flight-lines of the B4 survey along the southern San Andreas Fault (Bevis et al., 2005). Their ∼4–20 cm RMS errors therefore incorporate uncertainties in raw lidar point coordinates – which in the B4 survey were estimated at a few centimeters Toth et al. (2007) – and also account for the varying contributions of individual ground reflectors to each separate lidar survey. Nissen et al. (2012) also obtained similar RMS errors when applying ICP to point clouds deformed with a smoothly-varying elastic displacement field, as would be expected around a large earthquake rupture. This implies that the ±50 cm-level scatter in the ICP displacement field of the Fukushima–Hamadori event is not principally caused by internal deformation of cell topography arising from steep deformation gradients. It is also unlikely to reflect ambiguities in aligning planar cell surfaces, given the short-wavelength relief observed across the scene (Fig. 5b).

However, the B4 dataset incorporated into the Nissen et al. (2012) experiments – a 'geodetic-grade' survey designed for earthquake applications – differs from the third party surveys used in this study in a number of important respects: (1) The Nissen et al. (2012) B4-derived synthetic pre- and post-event datasets had an average point density of ∼2 points/m^2, eight times that of the pre-event DTMs used in this study and twice that of the post-event DTMs. Clearly, higher point densities enable displacements

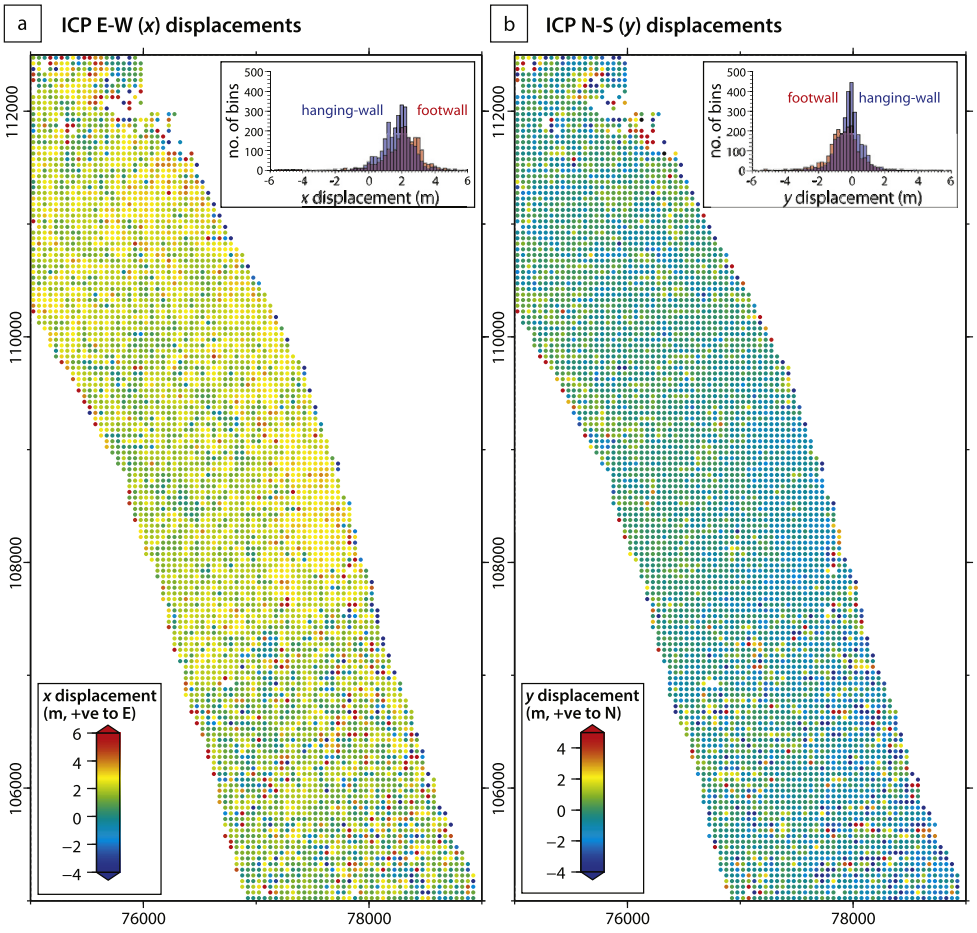

Fig. 7. (a) Fukushima–Hamadori earthquake *x*-axis displacements (positive is to the E) from ICP differencing. The entire field shows East displacement of ∼2 m caused by upper plate deformation of the 2011 Great Tohoku subduction earthquake. Inset shows a histogram of *x* displacement values, constructed using a bin width of 0.2 m and separated into footwall in red and hanging-wall in blue. (b) *y*-axis displacements (positive is to the North) with inset histogram as in (a). The lack of systematic variations in these horizontal displacements over the map area is consistent with predominantly dip slip along the steeply dipping fault zone. (For interpretation of the references to color in this figure legend, the reader is referred to the web version of this article.)

to be measured at greater precision. (2) The test area chosen by Nissen et al. (2012) in southern California contained only sparse, low-lying vegetation and there was consequently no need to strip canopy returns from the scenes. In our Japan examples, we are unsure exactly how the pre- and post-event bare Earth DTMs were constructed; the two lidar providers may have used different algorithms for stripping vegetation from the scene which could translate into significant differences in the final DTM surfaces. Vegetation growth or decay in between the two lidar acquisitions could also potentially influence ICP displacements if canopy returns were not completely removed during DTM construction. (3) Aircraft trajectories during each separate B4 flight were tied to the same differential GPS base stations, minimizing positioning errors. In contrast, the survey pairs used in this study were flown by separate companies, years apart, using different GPS ground control. This may have resulted in much larger point positioning inconsistencies between the Japanese surveys than the decimeter-level uncertainties estimated for the B4 dataset (Shan et al., 2007). Furthermore, without additional data collection metrics it is impossible to assess errors in scanner pointing direction, range, aircraft orientation or trajectory. In the near future, reliance on the type of "legacy" datasets used to investigate the Iwate–Miyagi and Fukushima–Hamadori earthquakes – as well as the El Mayor–Cucapah event (Glennie et al., 2014) – may be the rule rather than the exception for lidar differencing studies. These earthquakes may therefore act as important precedents.

There is also much scope for improving and refining the methodology for determining 3-D deformation from paired lidar datasets. A "sliding window" approach – coupled with careful filtering – could potentially be used to remove some of the noise, and other variants of ICP could also be tested (e.g., Rusinkiewicz and Levoy, 2001), including ones which incorporate spot height errors (Glennie et al., 2014). Other topography differencing techniques are also available including DEM pixel tracking (Leprince et al., 2012), point cloud cross-correlation (Borsa and Minster, 2012), and particle image velocimetry (Mukoyama, 2012; Aryal et al., 2012). There is potential in all of these methods to include the intensity values of the lidar returns as an additional constraint on horizontal displacements – as discussed by Borsa and Minster (2012) – although this adaptation is perhaps best suited to areas with sparser vegetation than in our Japan examples. Other algorithms that register point clouds or DTMs using non-rigid body transformations could potentially also be adapted for earthquake studies, helping account for any internal cell strains in addition to calculating translations and rotations (e.g., Rueckert et al., 1999; Lin et al., 2010; Wu et al., 2013). Finally, the Japan examples also illustrate how by integrating a simple DTM elevation differencing approach, localized mass movements can be easily distinguished from the smoother coseismic displacement field. More sophisticated elevation differencing algorithms could also be incorporated, such as those which account for DTM uncertainties or differences in point cloud roughnesses (Wheaton et al., 2010; Lague et al., 2013).

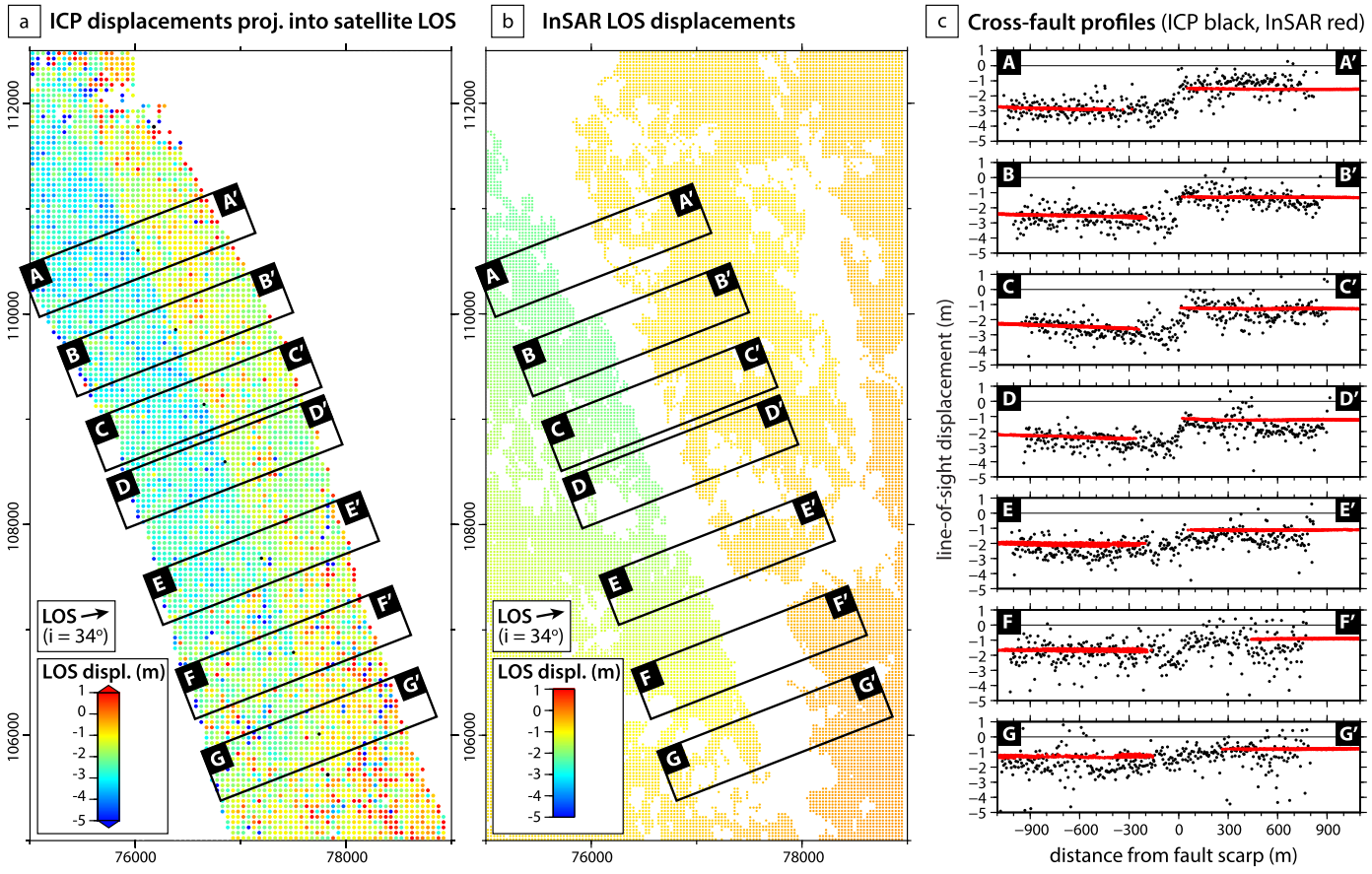

Fig. 8. (a) ICP displacement results resolved into the InSAR satellite line-of-sight (LOS). These are calculated by projecting the combined ICP translation for each cell ($t_x + t_y + t_z$) onto the pointing vector shown in Fig. 1c. In other words, $t_{LOS} = -(t_x \cdot \sin i \cdot \cos(360 - \phi)) - (t_y \cdot \sin i \cdot \sin(360 - \phi)) + (t_z \cdot \cos i)$ where t_x, t_y and t_z are translations in the x, y and z directions, i is the satellite center scene incidence angle of 34°, and ϕ is the ascending-track satellite azimuth of 346.9°. We classify positive LOS displacements as motion towards the satellite, i.e. a decrease in range. Positive t_x and t_y values increase the range and thus contribute negatively towards t_{LOS} whereas positive t_z decreases the range and thus contributes positively towards t_{LOS}. (b) Unwrapped InSAR LOS displacements, from the same interferogram as is shown in Fig. 1c. These displacements have been smoothed using an adaptive spatial filter (Goldstein and Werner, 1998) and the unfiltered interferograms contain additional noise on the level of a few centimeters. (c) Cross-fault swath profiles through the ICP LOS displacements (black) and filtered InSAR LOS displacements (red), from the areas shown in (a) and (b). The correspondence between the two completely independent datasets is remarkable and they have a useful complementarity between near (ICP) and far field (InSAR). (For interpretation of the references to color in this figure legend, the reader is referred to the web version of this article.)

4.2. Near fault displacements and shallow slip deficit

The vertical distribution of fault slip in large earthquakes places important constraints on the depth variation in mechanical properties (of the fault itself and of the surrounding volume), shaping our understanding of the earthquake cycle, the longer-term structural evolution of the fault zone, and the expression of active faulting in topography and geomorphology. Several studies have suggested that large events commonly exhibit a 'shallow slip deficit' in which inferences of near-surface slip – often based largely or entirely on field measurements of surface offset – are routinely lower than those of slip at depths of a few kilometers, usually determined with InSAR or other geodetic or seismological inversions (e.g., Simons et al., 2002; Fialko et al., 2005; Copley et al., 2012; Dolan and Haravitch, 2014). These patterns are best documented in strike-slip earthquakes, in which the most pronounced shallow slip deficits are associated with structurally-immature faults that have relatively small cumulative offsets (<10 km; Fialko et al., 2005; Dolan and Haravitch, 2014).

Many large earthquakes exhibit highly irregular surface offset distributions, much like the one shown in Figs. 5c and 5d along the Itozawa fault (e.g., Ambraseys and Tchalenko, 1972; McGill and Rubin, 1999; Barka et al., 2002; Haeussler et al., 2004; Xu et al., 2006; Elliott et al., 2012; Gold et al., 2013). This raises the question: how much of this variability results from heterogeneous subsurface slip and how much instead reflects the fact that while field measurements are made only on visible scarps or ruptures, the total offset might be accommodated across broader zones of distributed slip or warping? The 1999 Izmit (Turkey) and 2010 Darfield (New Zealand) strike-slip earthquakes, for instance, generated 30–300 m-wide inflections to linear rows of trees or crops, fences, and other cultural features which imply non-brittle rupture and off-fault deformation in the shallow subsurface (Rockwell et al., 2002; Quigley et al., 2010). In contrast, offsets to linear agricultural features generated by the 1940 Imperial Valley earthquake (California) are localized to within just ~5 m of the primary rupture yet also exhibit a high degree of short-wavelength, along-strike variability (Rockwell and Klinger, 2013).

Clearly, this question has important implications for how shallow slip deficits in large events are inferred and interpreted. Unfortunately, many coseismic SAR interferograms decorrelate along surface ruptures (within a kilometer or so of the fault break) due to the steep phase gradients (e.g., Figs. 1b, 1c) and consequently there is often a critical observational gap between measurements taken at the fault scarp and those in the far-field. In the Fukushima–Hamadori earthquake, however, lidar differencing provides unique constraints on this near-field deformation and thus on fault slip in at depths of a few tens to several hundreds of meters. Calculation of the near-surface slip distribution is beyond the scope of this paper – though it is clearly feasible using data of the kind presented

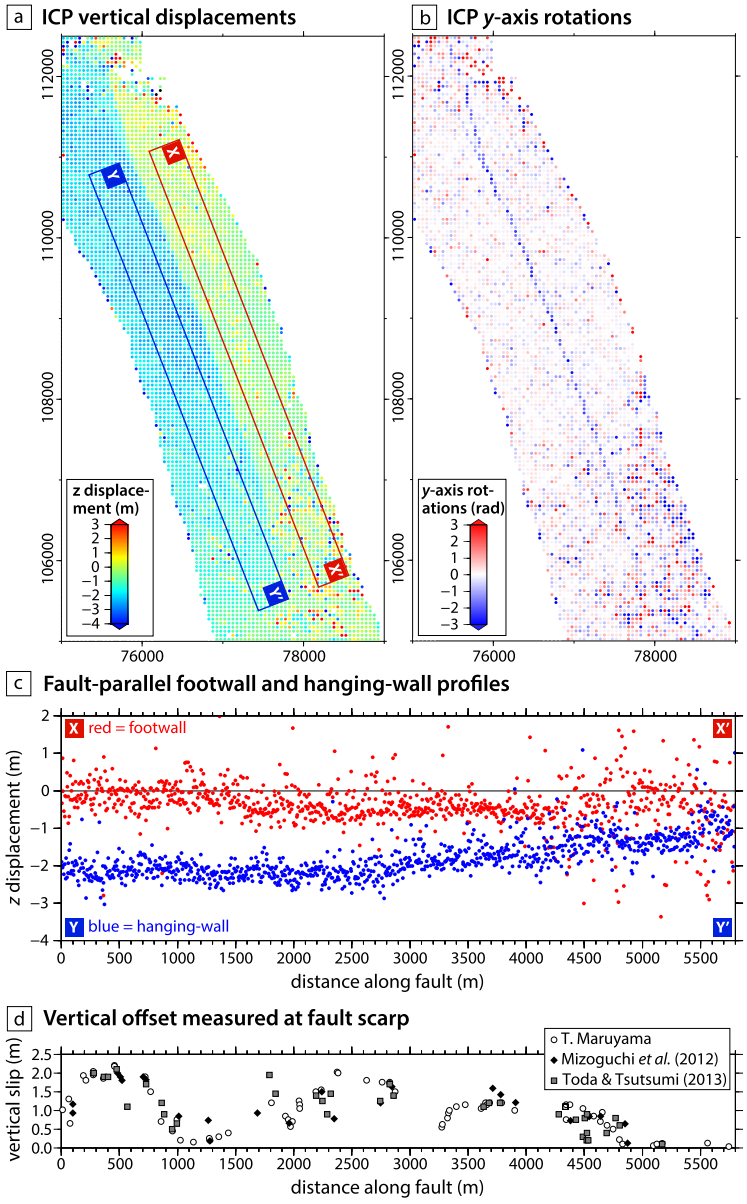

Fig. 9. (a) Vertical displacements obtained through ICP differencing of pre- and post-event DTMs (these are the same results as plotted in Fig. 6b). (b) *y*-axis rotations (positive is clockwise about the positive axis). (c) Fault-parallel profiles through ICP vertical displacements in the footwall (red) and hanging-wall (blue). The area included in each profile is shown in the same color in (a). (d) Field measurements of vertical surface offset by T. Maruyama, Mizoguchi et al. (2012) and Toda and Tsutsumi (2013), projected onto the same fault-parallel profile as in (c). Although the maxima in the fault parallel ICP profiles and the surface offset measurements are similar, the latter are much more irregular along the length of the rupture. This implies that fault slip "bleeds off" irregularly in the upper few hundred meters of the fault zone. (For interpretation of the references to color in this figure legend, the reader is referred to the web version of this article.)

here – but in this case even a qualitative assessment of the lidar deformation field is informative.

Cross-fault swath profiles through the ICP vertical displacements (Fig. 6c) appear to show inflections close to the surface rupture that reflect up-dip slip decrease (if the slip were uniform all the way to the surface then there would instead be a discrete discontinuity or step in displacements at the fault). The precise width of the inflection is difficult to discern from these profiles due to scatter but appears no larger than ~200 m. At greater distances away from the fault, such as the 200–600 m distances sampled in the fault-parallel swath profiles shown in Figs. 9a and 9c, the differences between footwall and hanging-wall vertical displacements appear to remain a roughly constant ~2 m along the northern half of the study area zone – similar in magnitude to the maximum surface offsets observed in the field – before gradually decaying southwards. These wider aperture displacement measurements are indicative of fault slip at a few hundred meters depth. Although short-wavelength, subsurface slip heterogeneities may be partially smoothed over in the surface deformation field, the profile shown in Fig. 9c still implies that slip at these depths is much more uniform than the highly fluctuating surface faulting offsets shown in Fig. 9d. Only the very largest vertical surface offsets measured in the field appear consistent with the slip magnitude inferred from the profiles in Fig. 9c.

ICP rotation results provide even tighter constraints on the depth extents over which large fault slip heterogeneities occur (Fig. 9b). A narrow band of pixels containing large anticlockwise rotations about the positive *y*-axis (the horizontal axis pointing N) delineates the entire length of the surface rupture and represent the up-to-the-East surface faulting or warping within these cells. These large rotation values are confined to single cells even along those fault sections which exhibit small surface offsets, implying

that most of the near-surface depletion in slip originates within a few tens of meters of the surface.

This very shallow slip depletion may reflect (1) large near-surface slip gradients that are recovered by creep later on in the earthquake cycle, (2) loss of slip to near-surface folding, or (3) redistribution of slip onto smaller subsidiary faults and fractures that were too subtle to have been observed in the field. Interestingly, some of the greatest surface offsets occur within a small sedimentary basin whereas some of the conspicuously small offsets occur where the surface is mantled with relatively thin colluvium. This suggests that any loss of primary fault slip occurs within bedrock, rather than in unconsolidated sediment as was the case in the Izmit and Darfield earthquakes (Rockwell et al., 2002; Quigley et al., 2010). The coseismic reversal of local topography along the Itozawa fault implies a small total throw on a structurally immature fault (Mizoguchi et al., 2012; A. Lin et al., 2013; Toda and Tsutsumi, 2013). We do not observe any clear, generalized lithological or geomorphological differences between areas with large surface slip deficit and those with no difference between surface slip and that detected with differential lidar.

5. Conclusions

We apply the Iterative Closest Point technique to two pairs of high-resolution lidar-derived DTMs spanning earthquake surface ruptures in forested uplands of Honshu, Japan. Differencing of pre- and post-earthquake DTMs recover coherent displacements across rupture zones of the 14 June 2008 Iwate–Miyagi (M_w 6.9, reverse sense) and 11 April 2011 Fukushima–Hamadori (M_w 7.1, normal sense) earthquakes. Resulting 3-D displacement fields show significant noise (at a roughly $\pm$50 cm level) but nevertheless yield valuable information about near-field deformation and shallow fault slip. Along the Itozawa rupture in the Fukushima–Hamadori earthquake, our ICP results imply that fault slip varies smoothly below shallow depths of a few tens of meters. Field observations of meter-scale fluctuations in fault offset over short ($<$1 km) strike distances are therefore likely to reflect a redistribution of primary fault slip onto subsidiary structures or into folding close to the surface. Field observations and lidar differencing results are insufficient to conduct such a test for the Iwate–Miyagi earthquake, though the coherency of lidar differencing results in the area examined again suggests that fault slip also varies smoothly below any shallow subsurface complexity. Together, these results demonstrate the potential for differencing of lidar-derived terrain models to enhance understanding of fault slip, especially in the near field and in densely vegetated terrain where other remote-sensing techniques struggle to recover displacement.

Acknowledgements

We are very grateful to Kokusai Kogyo Co., Ltd., and Aero Asahi Corp. for granting us access to their commercial lidar datasets and we appreciate their interest in our work. This project is primarily supported by the Southern California Earthquake Center (SCEC) through the Virtual Institute for the Study of Earthquake Systems (VISES) and SCEC Award 14101. Portions of the research were motivated and supported by a USGS cooperative grant awarded to E.N. (G12AC20042) and a National Science Foundation grant awarded to J.R.A., M.E.O. and S.S. (EAR-1148302). E.N. was also supported during the early stages of this project by an Exploration Fellowship from the School of Earth and Space Exploration at Arizona State University. J.R.E. is supported by the UK Natural Environmental Research Council (NERC) through the Earthquake without Frontiers (EwF) project (EwF NE/J02001X/1 1), NCEO (R8/H12/82) and the Centre for the Observation and Modelling of Earthquakes, Volcanoes and Tectonics (COMET+). We thank two anonymous reviewers for their helpful feedback, and we are also grateful to all those involved in the VISES workshop in Tokyo in November 2013 with whom we discussed this work, in particular Koji Okumura, Chris Crosby, Yuichi Hayakawa and Shinji Toda. Most of the figures in this paper were created using free Generic Mapping Tools software (Wessel et al., 2013).

References

Abe, T., Furuya, M., Takada, Y., 2013. Nonplanar fault source modeling of the 2008 M_w 6.9 Iwate–Miyagi Inland earthquake in Northeast Japan. Bull. Seismol. Soc. Am. 103 (1), 507–518.

Ambraseys, N.N., Tchalenko, J.S., 1972. Seismotectonic aspects of the Gediz, Turkey, earthquake of March 1970. Geophys. J. Int. 30 (3), 229–252.

Aryal, A., Brooks, B.A., Reid, M.E., Bawden, G.W., Pawlak, G.R., 2012. Displacement fields from point cloud data: application of particle imaging velocimetry to landslide geodesy. J. Geophys. Res. 117, F01029.

Barka, A., Akyüz, H.S., Altunel, E., Sunal, G., Cakir, Z., Dikbas, A., Yerli, B., Armijo, R., Meyer, B., de Chabalier, J.B., Rockwell, T., Dolan, J.R., Hartleb, R., Dawson, T., Christofferson, S., Tucker, A., Fumal, T., Langridge, R., Stenner, H., Lettis, W., Bachhuber, J., Page, W., 2002. The surface rupture and slip distribution of the 17 August 1999 Izmit earthquake (M 7.4), North Anatolian fault. Bull. Seismol. Soc. Am. 92 (1), 43–60.

Barth, N.C., Toy, V.G., Langridge, R.M., Norris, R.J., 2012. Scale dependence of oblique plate-boundary partitioning: new insights from LiDAR, central Alpine fault, New Zealand. Lithosphere 4 (5), 435–448.

Besl, P.J., McKay, N.D., 1992. A method for registration of 3-D shapes. IEEE Trans. Pattern Anal. Mach. Intell. 14 (2), 239–256.

Bevis, M., Hudnut, K., Sanchez, R., Toth, C., Grejner-Brzezinska, D., Kendrick, E., Caccamise, D., Raleigh, D., Zhou, H., Shan, S., Shindle, W., Yong, A., Harvey, J., Borsa, A., Ayoub, F., Shrestha, R., Carter, B., Sartori, M., Phillips, D., Coloma, F., 2005. The B4 project: scanning the San Andreas and San Jacinto fault zones. AGU Fall Meeting Abstracts, H34–B01.

Borsa, A., Minster, J.B., 2012. Rapid determination of near-fault earthquake deformation using differential lidar. Bull. Seismol. Soc. Am. 102, 1335–1347.

Carter, W.E., Shrestha, R.L., Slatton, K.C., 2007. Geodetic laser scanning. Phys. Today 60, 41–47.

Chen, Y., Medioni, G., 1992. Object modelling by registration of multiple range images. Image Vis. Comput. 10 (3), 145–155.

Copley, A., Hollingsworth, J., Bergman, E., 2012. Constraints on fault and lithosphere rheology from the coseismic slip and postseismic afterslip of the 2006 Mw 7.0 Mozambique earthquake. J. Geophys. Res. 117, B03404.

Cunningham, D., Grebby, S., Tansey, K., Gosar, A., Kastelic, V., 2006. Application of airborne LiDAR to mapping seismogenic faults in forested mountainous terrain, southeastern Alps, Slovenia. Geophys. Res. Lett. 33, L20308.

Dolan, J.F., Haravitch, B.D., 2014. How well do surface slip measurements track slip at depth in large strike-slip earthquakes? The importance of fault structural maturity in controlling on-fault slip versus off-fault surface deformation. Earth Planet. Sci. Lett. 388, 38–47.

Elliott, J.R., Nissen, E.K., England, P.C., Jackson, J.A., Lamb, S., Li, Z., Oehlers, M., Parsons, B., 2012. Slip in the 2010–2011 Canterbury earthquakes, New Zealand. J. Geophys. Res. 117, B03401.

Fialko, Y., 2004. Probing the mechanical properties of seismically active crust with space geodesy: study of the coseismic deformation due to the 1992 M_w 7.3 Landers (southern California) earthquake. J. Geophys. Res. 109, B03307.

Fialko, Y., Sandwell, D., Simons, M., Rosen, P., 2005. Three-dimensional deformation caused by the Bam, Iran, earthquake and the origin of shallow slip deficit. Nature 435, 295–299.

Fukushima, Y., Takada, Y., Hashimoto, M., 2013. Complex ruptures of the 11 April 2011 M_w 6.6 Iwaki earthquake triggered by the 11 March 2011 M_w 9.0 Tohoku earthquake, Japan. Bull. Seismol. Soc. Am. 103 (2B), 1572–1583.

Glennie, C.L., Carter, W.E., Shrestha, R.L., Dietrich, W.E., 2013. Geodetic imaging with airborne LiDAR: the Earth's surface revealed. Rep. Prog. Phys. 76 (8), 086801.

Glennie, C.L., Hinojosa-Corona, A., Nissen, E., Kusari, A., Oskin, M.E., Arrowsmith, J.R., Borsa, A., 2014. Optimization of legacy LiDAR datasets for measuring near-field earthquake displacements. Geophys. Res. Lett. 41 (10), 3494–3501.

Gold, P.O., Oskin, M.E., Elliott, A.J., Hinojosa-Corona, A., Taylor, M.H., Kreylos, O., Cowgill, E., 2013. Coseismic slip variation assessed from terrestrial lidar scans of the El Mayor–Cucapah surface rupture. Earth Planet. Sci. Lett. 366, 155–162.

Goldstein, R.M., Werner, C.L., 1998. Radar interferogram filtering for geophysical applications. Geophys. Res. Lett. 25, 4035–4038.

Haeussler, P.J., Schwartz, D.P., Dawson, T.E., Stenner, H.D., Lienkaemper, J.J., Sherrod, B., Cinti, F.R., Montone, P., Craw, P.A., Crone, A.J., Personius, S.F., 2004. Surface rupture and slip distribution of the Denali and Totschunda faults in the 3 November 2002 M 7.9 earthquake, Alaska. Bull. Seismol. Soc. Am. 94 (6B), S23–S52.

Haugerud, R.A., Harding, D.J., Johnson, S.Y., Harless, J.L., Weaver, C.S., Sherrod, B.L., 2003. High-resolution lidar topography of the Puget Lowland, Washington. GSA Today 13 (6), 4–10.

Hunter, L.E., Howle, J.F., Rose, R.S., Bawden, G.W., 2011. LiDAR-assisted identification of an active fault near Truckee, California. Bull. Seismol. Soc. Am. 101 (3), 1162–1181.

Imanishi, K., Ando, R., Kuwahara, Y., 2012. Unusual shallow normal-faulting earthquake sequence in compressional northeast Japan activated after the 2011 off the Pacific coast of Tohoku earthquake. Geophys. Res. Lett. 39, L09306.

Kato, A., Sakai, S., Obara, K., 2011. A normal-faulting seismic sequence triggered by the 2011 off the Pacific coast of Tohoku earthquake: wholesale stress changes in the upper plate. Earth Planets Space 63, 745–748.

Kobayashi, T., Tobita, M., Koarai, M., Okatani, T., Suzuki, A., Noguchi, Y., Yamanaka, M., Miyahara, B., 2012. InSAR-derived crustal deformation and fault models of normal faulting earthquake (Mj 7.0) in the Fukushima–Hamadori area. Earth Planets Space 64, 1209–1221.

Lague, D., Brodu, N., Leroux, J., 2013. Accurate 3D comparison of complex topography with terrestrial laser scanner: application to the Rangitikei canyon (NZ). ISPRS J. Photogramm. Remote Sens. 82, 10–26.

Langridge, R.M., Ries, W.F., Farrier, T., Barth, N.C., Khajavi, N., De Pascale, G.P., 2014. Developing sub 5-m LiDAR DEMs for forested sections of the Alpine and Hope faults, South Island, New Zealand: implications for structural interpretations. J. Struct. Geol. 64, 53–66.

Leprince, S., Hudnut, K.W., Akciz, S.O., Hinojosa-Corona, A., Fletcher, J.M., 2012. Surface rupture and slip variation induced by the 2010 El Mayor–Cucapah earthquake, Baja California, quantified using COSI-Corr analysis on pre- and post-earthquake LiDAR acquisitions. AGU Fall Meeting Abstracts, EP41A–0596.

Lin, A., Toda, S., Rao, G., Tsuchihashi, S., Yan, B., 2013. Structural analysis of coseismic normal fault zones of the 2011 M_w 6.6 Fukushima earthquake, Northeast Japan. Bull. Seismol. Soc. Am. 103 (2B), 1603–1613.

Lin, S.Y., Muller, J.P., Mills, J.P., Miller, P.E., 2010. An assessment of surface matching for the automated co-registration of MOLA, HRSC and HiRISE DTMs. Earth Planet. Sci. Lett. 294 (3), 520–533.

Lin, Z., Kaneda, H., Mukoyama, S., Asada, N., Chiba, T., 2013. Detection of subtle tectonic–geomorphic features in densely forested mountains by very high-resolution airborne LiDAR survey. Geomorphology 182, 104–115.

Lucca, E., Festa, G., Emolo, A., 2012. Kinematic inversion of strong-motion data using a Gaussian parameterization for the slip: application to the 2008 Iwate–Miyagi, Japan, earthquake. Bull. Seismol. Soc. Am. 102 (6), 2685–2703.

Massonnet, D., Rossi, M., Carmona, C., Adragna, F., Peltzer, G., Feigl, K., Rabaute, T., 1993. The displacement field of the Landers earthquake mapped by radar interferometry. Nature 364 (6433), 138–142.

Matsu'ura, T., Kase, Y., 2010. Late Quaternary and coseismic crustal deformation across the focal area of the 2008 Iwate–Miyagi Nairiku earthquake. Tectonophysics 487, 13–21.

McGill, S.F., Rubin, C.M., 1999. Surficial slip distribution on the central Emerson fault during the June 28, 1992, Landers earthquake, California. J. Geophys. Res. 104 (B3), 4811–4833.

Michel, R., Avouac, J.P., Taboury, J., 1999. Measuring ground displacements from SAR amplitude images: application to the Landers earthquake. Geophys. Res. Lett. 26 (7), 875–878.

Midorikawa, S., Miura, H., 2008. Damage and high-resolution SAR image in the 2008 Iwate–Miyagi–Nairiku, Japan earthquake. In: 6th International Workshop on Remote Sensing for Disaster Applications.

Mizoguchi, K., Uehara, S., Ueta, K., 2012. Surface fault ruptures and slip distributions of the M_w 6.6 11 April 2011 Hamadori, Fukushima Prefecture, Northeast Japan, Earthquake. Bull. Seismol. Soc. Am. 102, 1949–1956.

Mukoyama, S., 2012. Estimation of ground deformation caused by the earthquake (M_w 7.2) in Japan, 2008, from the geomorphic image analysis of high resolution LiDAR DEMs. J. Mt. Sci. 8, 239–245.

Nakata, T., Imaizumi, T., 2002. Digital Active Fault Map of Japan. University of Tokyo Press (in Japanese).

Nissen, E., Krishnan, A.K., Arrowsmith, J.R., Saripalli, S., 2012. Three-dimensional surface displacements and rotations from differencing pre- and post-earthquake LiDAR point clouds. Geophys. Res. Lett. 39, L16301.

Ohta, Y., Ohzono, M., Miura, S., Iinuma, T., Tachibana, K., Takatsuka, K., Miyao, K., Sato, T., Umino, N., 2008. Coseismic fault model of the 2008 Iwate–Miyagi Nairiku earthquake deduced by a dense GPS network. Earth Planets Space 60 (12), 1197.

Oskin, M.E., Arrowsmith, J.R., Corona, A.H., Elliott, A.J., Fletcher, J.M., Fielding, E.J., Gold, P.O., Garcia, J.J.G., Hudnut, K.W., Liu-Zeng, J., Teran, O.J., 2012. Near-field deformation from the El Mayor–Cucapah earthquake revealed by differential LiDAR. Science 335, 702–705.

Ozawa, S., Nishimura, T., Suito, H., Kobayashi, T., Tobita, M., Imakiire, T., 2011. Coseismic and postseismic slip of the 2011 magnitude-9 Tohoku–Oki earthquake. Nature 475 (7356), 373–376.

Prentice, C.S., Crosby, C.J., Whitehill, C.S., Arrowsmith, J.R., Furlong, K.P., Phillips, D.A., 2009. Illuminating Northern California's active faults. Eos Trans. AGU 90, 55.

Quigley, M., van Dissen, R., Villamor, P., Litchfield, N., Barrell, D., Furlong, K., Stahl, T., Duffy, B., Bilderback, E., Noble, D., Townsend, D., Begg, J., Jongens, R., Ries, W., Claridge, J., Klahn, A., Mackenzie, H., Smith, A., Hornblow, S., Nicol, R., Cox, S., Langridge, R., Pedley, K., 2010. Surface rupture of the Greendale fault during the Darfield (Canterbury) earthquake, New Zealand: initial findings. Bull. N. Z. Soc. Earthq. Eng. 43 (4), 236–242.

Rockwell, T., Klinger, Y., 2013. Surface rupture and slip distribution of the 1940 Imperial Valley earthquake, Imperial Fault, Southern California: implications for rupture segmentation and dynamics. Bull. Seismol. Soc. Am. 103 (2A), 629–640.

Rockwell, T.K., Lindvall, S., Dawson, T., Langridge, R., Lettis, W., Klinger, Y., 2002. Lateral offsets on surveyed cultural features resulting from the 1999 Izmit and Düzce earthquakes, Turkey. Bull. Seismol. Soc. Am. 92 (1), 79–94.

Rueckert, D., Sonoda, L.I., Hayes, C., Hill, D.L., Leach, M.O., Hawkes, D.J., 1999. Non-rigid registration using free-form deformations: application to breast MR images. IEEE Trans. Med. Imaging 18 (8), 712–721.

Rusinkiewicz, S., Levoy, M., 2001. Efficient variants of the ICP algorithm. In: Proceedings Third International Conference on 3-D Digital Imaging and Modeling, pp. 145–152.

Shan, S., Bevis, M., Kendrick, E., Mader, G.L., Raleigh, D., Hudnut, K., Sartori, M., Phillips, D., 2007. Kinematic GPS solutions for aircraft trajectories: identifying and minimizing systematic height errors associated with atmospheric propagation delays. Geophys. Res. Lett. 34, L23S07.

Simons, M., Fialko, Y., Rivera, L., 2002. Coseismic deformation from the 1999 M_w 7.1 Hector Mine, California, earthquake as inferred from InSAR and GPS observations. Bull. Seismol. Soc. Am. 92 (4), 1390–1402.

Suzuki, W., Aoi, S., Sekiguchi, H., 2012. Rupture process of the 2008 Iwate–Miyagi Nairiku, Japan, earthquake derived from near-source strong-motion records. Bull. Seismol. Soc. Am. 100 (1), 256–266.

Takada, Y., Kobayashi, T., Furuya, M., Murakami, M., 2009. Coseismic displacement due to the 2008 Iwate–Miyagi Nairiku earthquake detected by ALOS/PALSAR: preliminary results. Earth Planets Space 61, 9–12.

Teza, G., Galgaro, A., Zaltron, N., Genevois, R., 2007. Terrestrial laser scanner to detect landslide displacement fields: a new approach. Int. J. Remote Sens. 28 (16), 3425–3446.

Toda, S., Maruyama, T., Yoshimi, M., Kaneda, H., Awata, Y., Yoshioka, T., Ando, R., 2012. Surface rupture associated with the 2008 Iwate–Miyagi Nairiku, Japan, earthquake and its implications to the rupture process and evaluation of active faults. Jishin 2 (J. Seismol. Soc. Jpn.) 62, 153–178 (in Japanese with English abstract).

Toda, S., Tsutsumi, H., 2013. Spontaneous reactivation of two, subparallel, inland normal faults during the M_w 6.6 11 April 2011 Iwaki earthquake triggered by the M_w 9.0 Tohoku-oki, Japan, earthquake. Bull. Seismol. Soc. Am. 103 (2B), 1584–1602.

Toth, C., Brzezinska, D., Csanyi, N., Paska, E., Yastikli, N., 2007. LiDAR mapping supporting earthquake research of the San Andreas fault. In: Proceedings of the ASPRS 2007 Annual Conference. American Society for Photogrammetry and Remote Sensing, pp. 1–11.

van Puymbroeck, N., Michel, R., Binet, R., Avouac, J.P., Taboury, J., 2000. Measuring earthquakes from optical satellite images. Appl. Opt. 39 (20), 3486–3494.

Wessel, P., Smith, W.H., Scharroo, R., Luis, J., Wobbe, F., 2013. Generic mapping tools: improved version released. Eos Trans. AGU 94 (45), 409–410.

Wheaton, J.M., Brasington, J., Darby, S.E., Sear, D.A., 2010. Accounting for uncertainty in DEMs from repeat topographic surveys: improved sediment budgets. Earth Surf. Process. Landf. 35, 136–156.

Wu, B., Guo, J., Hu, H., Li, Z., Chen, Y., 2013. Co-registration of lunar topographic models derived from Chang'E-1, SELENE, and LRO laser altimeter data based on a novel surface matching method. Earth Planet. Sci. Lett. 364, 68–84.

Xu, X., Yu, G., Klinger, Y., Tapponnier, P., Van Der Woerd, J., 2006. Reevaluation of surface rupture parameters and faulting segmentation of the 2001 Kunlunshan earthquake (M_w 7.8), northern Tibetan Plateau, China. J. Geophys. Res. 111, B05316.

Yagi, H., Sato, G., Higaki, D., Yamamoto, M., Yamasaki, T., 2009. Distribution and characteristics of landslides induced by the Iwate–Miyagi Nairiku earthquake in 2008 in Tohoku District, Northeast Japan. Landslides 6 (4), 335–344.

Yokota, Y., Koketsu, K., Hikima, K., Miyazaki, S.I., 2009. Ability of 1 Hz GPS data to infer the source process of a medium sized earthquake: the case of the 2008 Iwate Miyagi Nairiku, Japan, earthquake. Geophys. Res. Lett. 36, L12301.